ECHELLE SPECTROSCOPY OF γ-RAY BINARY 1FGL J1018.6−5856

IDEL R. WAISBERG[1] AND ROGER W. ROMANI[1]
Submitted to ApJ

ABSTRACT

We observed the *Fermi*-discovered γ-ray binary 1FGL J1018.6−5856 at 20 epochs over 50 days using the CHIRON spectrograph, obtaining spectra at $R \sim 25{,}000$ covering $\lambda\lambda 4090 − 8908$Å. The average spectrum confirms an O6 V((f)) spectral type and extinction $E(B − V) = 1.35 \pm 0.04$. Variable absorption line equivalent widths suggest substantial contamination by wind line features. The limited S/N ratio hindered accurate continuum definition and prevented measurement of a high quality radial velocity curve. Nevertheless, the best data indicate a radial velocity amplitude $\leq 40 \mathrm{km\,s^{-1}}$ for the He II lines and substantially lower for H I. We argue that this indicates a most likely compact object mass $< 2.2 M_\odot$. While black hole solutions are not excluded, a neutron star source of the γ-ray emission seems preferred.

Subject headings: gamma rays: stars — binaries: spectroscopic

1. INTRODUCTION

To date only five binaries with high mass secondaries have been detected in the GeV band; 1FGL 1018.6−5856 is the only one whose binary period was discovered at these energies (Corbet et al. 2011; Ackerman et al. 2012). The nature of the γ-producing compact object in these binaries is unclear: it might be a jet-producing black hole, in analogy to γ-loud blazars (the 'μQSO model'), or the γ-rays may be generated by the magnetosphere or wind termination shock of an energetic pulsar (the 'PSR/PWN model'). This latter model certainly applies to the PSR B1259−63 system, whose GeV emission is produced via Inverse Compton scattering off wind shock particles when the PWN is compressed near periastron. For 1FGL 1018.6−5856 and the other three systems (LS I+61°303, LS 5039 and Cygnus X-3), the identity of the compact object is presently unknown. Discovery of γ-ray pulsations would certainly indicate a neutron star primary. However, the poorly known acceleration in the binaries makes γ-ray pulse searches prohibitively expensive and the dense plasma produced by the massive secondary winds frustrates radio pulse searches. An alternative approach is to constrain the compact object mass via measurement of the secondary's radial velocity. Although the high mass and strong winds of the secondary also make this very challenging, even crude constraints can be useful; for example a minimum companion mass $> 3 M_\odot$ would certainly indicate a black hole.

After discovery of a 16.5 d γ-ray modulation (Corbet et al. 2011), the associated $Swift$ X-ray source was identified with a bright optical counterpart. A low resolution spectrum with the SAAO 1.9 m shows an O6V((f)) companion with an estimated mass $\approx 20 − 30 M_\odot$ and distance ≈ 5 kpc (Ackerman et al. 2012). This system is also a radio source and $Swift$ XRT (An et al 2013) and ATCA monitoring detect the orbital modulation in the X-ray and radio band, respectively. Optical photometric monitoring detects no variation, although present constraints are weak. These properties are similar to those of the more compact (P_b=3.9 d) γ-ray binary LS 5039. There spectroscopic and photometric studies (e.g. Sarty et al. 2011) indicate an O6.5V((f)) secondary, a substantial eccentricity $e = 0.24 \pm 0.08$, and a modest mass

function $f(m) = 0.0049 \pm 0.0006 M_\odot$. The limit on LS 5039's photometric variability, 2mmag, implies a high system inclination and/or a small compact object mass. Since the inclination is poorly determined, they can only conclude that $M_1 > 1.8 M_\odot$, allowing both black hole and neutron star solutions.

In this paper we describe a project to study the radial velocity of 1FGL 1018.6−5856 using echelle spectroscopy. We adopt the orbital period estimate of Coley et al. (2014) $P_b = 16.549 \pm 0.007$ d with epoch MJD 55403.3 ± 0.4 corresponding to the γ-ray peak described in Ackerman et al. (2012). An independent $Swift/Fermi$ analysis (An, priv. comm.) confirms this ephemeris. While our results appear to show systematic variation with orbital phase, it is unclear if we have isolated the true radial velocity curve. Nevertheless, our measurements improve the characterization of the companion star, limit the amplitude of its motion and point to the sort of observations needed for a definitive study.

2. OBSERVATIONS AND CALIBRATIONS

The 16.5 d binary period is particularly inconvenient, being too long to cover in a dedicated run, but too short for effective coverage with ad hoc $\sim$ monthly observations. The best solution was queue observing and we were awarded 25h of queue time (NOAO-11B-0092) on the CTIO 1.5 m using the CHIRON fiber-coupled echelle spectrograph (Schwab et al. 2010). 1FGL 1018.6−5856 is relatively faint for CHIRON at $V = 12.5$, so CHIRON was run in the slitless (2.5″ fiber aperture) mode for an effective resolution $R \sim 25{,}000$. The CCDs were binned 4×4 to maximize S/N and minimize readout time. The spectra covered $4090−8908$Å, with substantial order overlap except in the reddest orders.

Observations were attempted roughly every other night from March 02, 2012 (JD 2455989) to April 20, 2012 (JD 2456022). Four nights were lost to system failures and weather; spectra were obtained on 20 nights (Table 1). We requested 3×1000 s exposure on 1FGL 1018.6−5856, one night had only a single exposure. For each epoch we obtained ThAr arc exposures immediately before the target observations for wavelength calibration. For the first epoch only we also observed the flux standard HD60753. CHIRON was undergoing final commissioning during these observations, and the obtained S/N was substantially lower than predicted by

[1] Department of Physics, Stanford University, Stanford, CA 94305-4060, USA; rwr@astro.stanford.edu, idelw@stanford.edu

TABLE 1
CHIRON OBSERVATIONS

Date	Nexp	S/N$_{6000\text{Å}}$	ϕ_B
03/02	3	36	0.41
03/06	1	24	0.65
03/10	3	12	0.89
03/14	3	33	0.13
03/16	3	32	0.25
03/18	3	44	0.37
03/20	3	37	0.49
03/22	3	33	0.61
03/24	3	3	0.73
03/26	3	31	0.85
03/28	3	18	0.98
03/30	3	18	0.09
04/02	3	28	0.28
04/04	3	31	0.40
04/06	3	21	0.51
04/08	3	8	0.63
04/10	3	22	0.76
04/12	3	20	0.87
04/18	3	30	0.24
04/20	3	29	0.38

the design plots (predicted peak S/N/extracted pixel ~ 40 in each 1000s exposure). In practice, we obtained S/N/extracted pixel ~ 25 at the order peaks in our best exposures (in line with recent revised 6.5% instrument efficiency). More typical S/N/extracted pixel was ≈ 17, with a few epochs much worse. We were not able to ascertain from the night logs why the S/N on source varied so dramatically, although from the low apparent flux at some epochs, we suspect that poor transparency and imperfect fiber acquisition may play a role. In the end we analyzed the 17 epochs with S/N> 15 in the summed, combined spectra. These spectra sample four binary orbits.

Although the CHIRON data distribution included a standard pipeline extraction of the echelle spectra, this was optimized for the relatively red target stars of the instrument's principal (radial velocity planet search) program. This extraction covered $\lambda\lambda 4504 - 8908$Å (62 orders); for our blue 06V target 14 additional orders were measurable, extending the spectral coverage to 4090Å.

Standard CCD processing was performed with the IRAF package. A master bias was assembled and subtracted from the target, flat and lamp images. The spectra for each epoch cover 3200s. As this is only 0.2% of the orbital period, intra-epoch velocity smearing was negligible and the three target exposures for each night were median combined with average σ-clipping to increase S/N and reject cosmic ray events. Combined flat field images were also prepared for each night. These were used to define the apertures for each order. Sufficient inter-order pixels were available to define flanking 'background' windows for each order. A linear fit to these backgrounds was used as a local scattered light subtraction. All extractions were performed using variance weighting, modeled by the CCD read noise ($4.5e^-$) and gain ($1.3e^-$/ADU).

The extracted science spectra for each order were divided by the extracted flat spectrum. This removed the blaze function and summed pixel-to-pixel variations, while maintaining a relatively stable response from the smooth lamp spectrum. In principle, the true response could be determined from the standard star spectrum. In practice, for the queue-selected standard the tabulated fluxes were derived from a spectral model and were too sparse (10Å grid) to fit an accurate sensi-
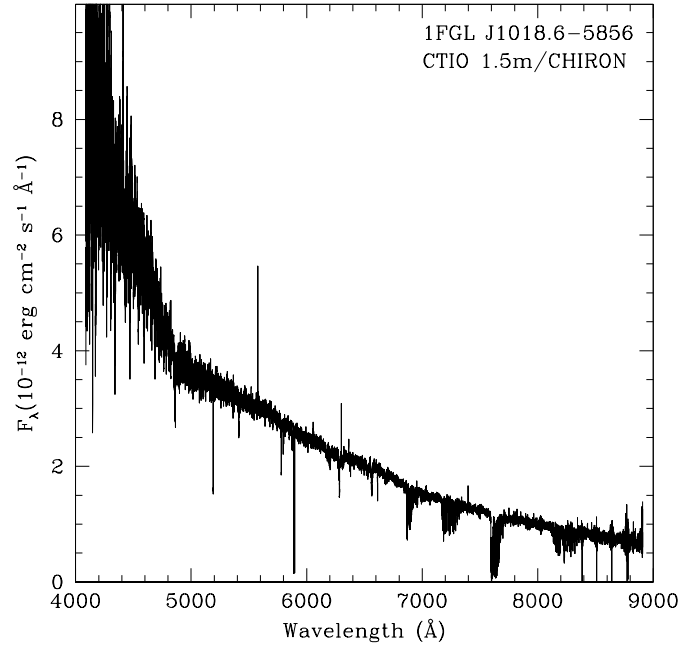

FIG. 1.— Fluxed CHIRON spectrum from March 02, 2012, corrected for atmospheric and interstellar ($E_{B-V} = 1.35$) extinction. Telluric features have not been removed. The strongest night sky and absorption lines are visible, along with inter-order gaps for the reddest five orders.

tivity function for each order. Accordingly we used the lamp-flattened spectra directly. The wavelength calibration was determined from the nightly ThAr spectra. Non-linear solutions were fit, with a typical rms residual 0.01Å. Note that although CHIRON is designed to be quite stable, night-to-night shifts in the spectrum position on the chip were significant. Aperture migrations (1-2 pixels) were treated by re-centering orders on the flat before extraction (and importing these traces to the arc and science spectra). Shifts along the dispersion direction (~ 0.1Å$\sim 5 - 10$km s^{-1}) were removed by running IRAF task *re-identify* on each night's ThAr arcs to derive the wavelength calibration.

After trimming very low S/N data at the edges of each echelle order, we merged all orders to a single spectrum, average-combining the overlap regions (figure 1). Given our relatively modest S/N for most of the spectra, this procedure generally produced an adequate match between orders. For some epochs, small flux gradients across orders and poor inter-order match were however present. Such imperfections can be attributed to differences in illumination paths of and/or light path shifts between flat and science images. These may be removed by computation of a smoothly varying residual blaze function (Skoda et al. 2008). Although we attempted such corrections, the S/N of our targets and standard exposures did not allow significant improvement. Finally, we divided the merged spectra by a low order function to remove the global lamp response and create normalized spectra appropriate to our kinematic/line study. The S/N weighted combined normalized spectrum from all epochs is shown in figure 2. An absolute fluxed spectrum was computed from the first night's data where the adjacent standard was used to normalize the fluxes. For each epoch we corrected the normalized spectrum to the heliocenter using the IRAF routines *rvcorrect* and *dopcor*.
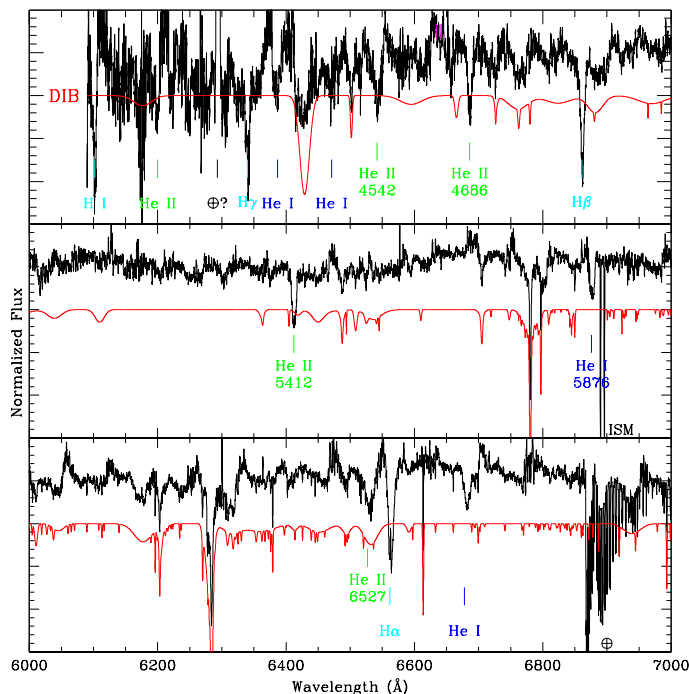
3. SPECTRUM ANALYSIS

FIG. 2.— Normalized average spectrum. Each sub-panel covers 1000Å. The strongest lines used for the radial velocity analysis are labeled, additional lines from these species are marked. The synthesized DIB transmission spectrum is generated from tables in Jenniskens et al. (1996) (normalized to $E_{B-V} = 1.35$) and is plotted offset by -0.1.

The overall spectrum (figure 1) is quite consistent with the SAAO spectrum of Ackerman et al. (2012), with H I, He I and He II lines competing with strong interstellar absorption. The He IIλ4541/He Iλ4471 ratio is a good diagnostic of subclass for O-type stars (Gray et al. 2009). From our combined spectrum we measure 2.3 ± 0.2 for this ratio, indicating O6 (Jaschek & Jaschek 1995). The N III emission line triplet 4634/4640/4642 is not present, or even weakly in absorption. Even higher S/N is needed to measure the state of this line. Its weakness argues for a dwarf classification; overall the designation O6 V((f)) is supported by this spectrum. The photospheric lines are broad, reaching FWHM 350 km s^{-1}. There were no sky fibers for sky subtraction and so a few of the brightest night sky lines (e.g. 5577Å) are visible. A broad emission feature at 4293Å appears in most of the spectra, with highly variable flux and high equivalent width even when the target was weak. As this corresponds to no strong astronomical line, we suspect a spectrograph artifact from local light. In figure 2 we label the strongest photospheric features.

3.1. *Interstellar Absorption*

Our measurement of the photospheric features is complicated by particularly strong interstellar absorption. Atomic features (e.g. Mg I 5174, Na I 5892) provide narrow absorptions, while Diffuse Interstellar Bands (DIBs) are particularly prominent in the spectrum. To identify these, we use the catalog of Jenniskens et al. (1996, see also http://leonid.arc.nasa.gov/DIBcatalog.html) to synthesize a DIB absorption spectrum, combining Gaussian features at the cataloged $\lambda_{\rm eff}$, kinematic and relative equivalent widths (figure 2). Comparison with the companion spectrum shows that many subtle broad features have a DIB origin. Note that the relative feature strength shown here is only typical; substantial variation exists between various Galactic sight-lines. The many DIB features make

TABLE 2
REDDENING FROM DIB MEASUREMENTS

DIB Å	$a^{\dagger}$	$b^{\dagger}$	EW Å	E_{B-V}
5780	0.506 ± 0.050	-0.014 ± 0.032	0.709 ± 0.009	1.43 ± 0.16
5797	0.124 ± 0.014	-0.003 ± 0.009	0.134 ± 0.006	1.10 ± 0.14
6196	0.048 ± 0.004	0.001 ± 0.003	0.063 ± 0.005	1.29 ± 0.12
6379	0.057 ± 0.012	0.004 ± 0.008	0.119 ± 0.005	2.00 ± 0.44
6613	0.192 ± 0.026	0.003 ± 0.017	0.225 ± 0.006	1.16 ± 0.18
6660	0.014 ± 0.004	0.009 ± 0.003	0.043 ± 0.004	2.54 ± 0.82

† Coefficients from Kos et al. (2013).

it particularly challenging to define the true photospheric continuum, in turn this can subtly affect our line centroid estimates.

The DIBs are believed to be generated by PAHs associated with interstellar dust. Thus one expects a correlation between DIB strength and interstellar reddening from dust scattering. Kos et al. (2013) lists fit linear relations for several strong DIBs of the form $EW = a \times E_{B-V} + b$. These relations depend on whether the sight-line is 'UV shielded' (ζ sight-line) or not (σ sight-line), and the $\lambda5797/\lambda5780$ EW ratio is used to discriminate these cases. Our value is 0.19 ± 0.01, below the 0.3 threshold, so we treat this as a σ sight-line. In table 2 we apply the tabulated coefficients to several well-measured DIBs to estimate the reddening. The inferred E_{B-V} have a surprisingly large scatter, with a weighted average $E_{B-V} = 1.35 \pm 0.04$ (bootstrap error). This value agrees very well with the estimate $E_{B-V} = 1.34 \pm 0.04$ determined by Napoli et al. (2011) from Strömgren photometry. It is similarly in reasonable accord with the N_H estimated from the X-ray spectrum. In turn, this agreement supports the photometric distance estimate $d = 5^{+4.6}_{-2.1}$ kpc.

3.2. *Radial Velocity Measurements*

To confirm the stability of our wavelength solutions, we measured the night sky lines $\lambda5577.3387$ Å and $\lambda6300.304$ Å in each processed spectrum, before heliocentric corrections were applied. The rms wavelength variations were 0.0106 Å and 0.0124 Å respectively, i.e. $\sigma_{RV} = 0.6$km s^{-1}.

A second stability check was made measuring the very strong Na(D) interstellar doublet $\lambda5889.951/5895.924$ Å in spectra corrected to the heliocenter. The line centroids display mean redshifts of 2.88 and 2.85 km s^{-1}, with spectrum-to-spectrum rms variation of 0.88 and 0.74km s^{-1}, respectively. We conclude that our wavelength solutions are good to better than 1 km s^{-1}.

To attempt to measure the photospheric velocity of the companion, we must follow the centroids of the broad ($\sim$ 300km s^{-1}) H I, He I and He II lines, to a few km s^{-1}. This is challenging since the imperfect inter-order fluxing causes significant gradients and steps in the continuum, with a characteristic scale comparable to the typical 50Å (3000 km s^{-1}) order width. Further, for several of the photospheric lines there are strong DIBs in the line wings, which can perturb the continuum. To mitigate this latter effect, we divide the spectrum by the model DIB spectrum. While imperfectly removing all DIBs, this does significantly flatten the continuum in the region of the strongest features.

All photospheric lines were fit with simple Gaussian profiles (test Voigt fitting showed negligible Lorentzian wings). The fitting used the IRAF deblending routine, where the ef-
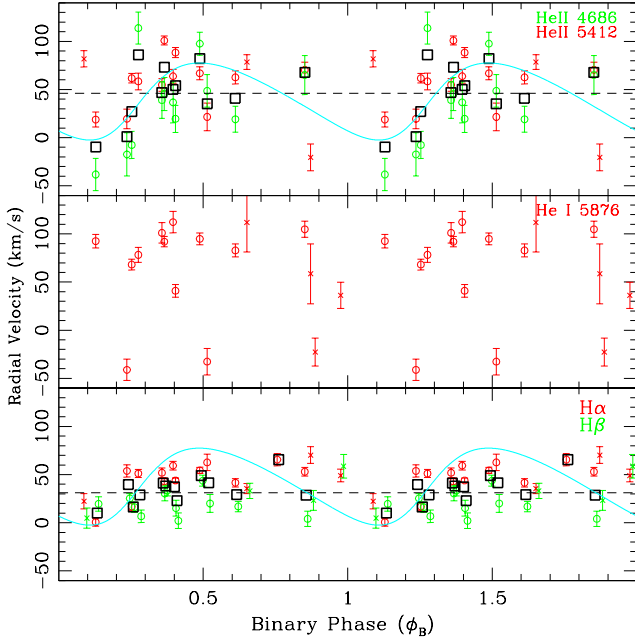
FIG. 3.— Radial Velocity measurements for three species. Points with circles are from high S/N spectra; those with crosses from lower S/N data. Black squares show the mean velocity of the two strongest lines for H I and He II for the high S/N spectra; large systematic scatter is seen. The sample $K = 40\,\mathrm{km\,s^{-1}}$ radial velocity curve plotted provides a reasonable match to the He II average points; the H I amplitude is $\sim 2.5\times$ smaller (see text).

fective noise was determined for each line by a measurement of the spectrum rms in the nearby, line-free continuum. The statistical errors on the fit parameters (line centroid, strength and, optionally kinematic width) are provided by the routine, based on Monte Carlo simulations. For the lower S/N lines the kinematic width was held fixed at the value measured from the average spectrum (5-10Å FWHM).

We also attempted to determine the line centroids using the so-called "mirroring" method (Parimucha & Skoda 2008). This allows one to separately probe the line wings and core. Although we can see that our lines are significantly asymmetric, suggesting absorption in wind/outflow components, we lacked the S/N to measure these structures accurately and compare them across lines and species. This prevented us from using the line shapes to improve our estimate of the systematic (photospheric) radial velocity.

4. RADIAL VELOCITY VARIATIONS

To test for velocity variation, we performed a weighted least-squares fit for the mean velocity of each species. Table 3 shows the velocities, errors, goodness of fit and the probability of constancy. It is unclear how to compare mean velocities between lines, as the effective rest wavelengths depend on the excitation. Also, the measured line centers are somewhat uncertain due to continuum irregularities; for example He II 6527 appears substantially redshifted, due to a continuum gradient and superposed DIB. Finally, the lower excitation lines can be affected by wind absorption and may be blue shifted with respect to He II (Casares et al. 2005; Sarty et al. 2011).

Overall, we infer a net systemic radial velocity of $\sim 40\,\mathrm{km\,s^{-1}}$, but a precise value requires cross-correlation with a simultaneously observed RV standard of similar spectral class. The reduced χ^2 values are, however, interesting. From the low probabilities, we infer that the the strong lines do indeed show statistically significant variation.

However, there are certainly large systematic effects, and it

TABLE 3
TEST FOR RADIAL VELOCITY VARIATIONS

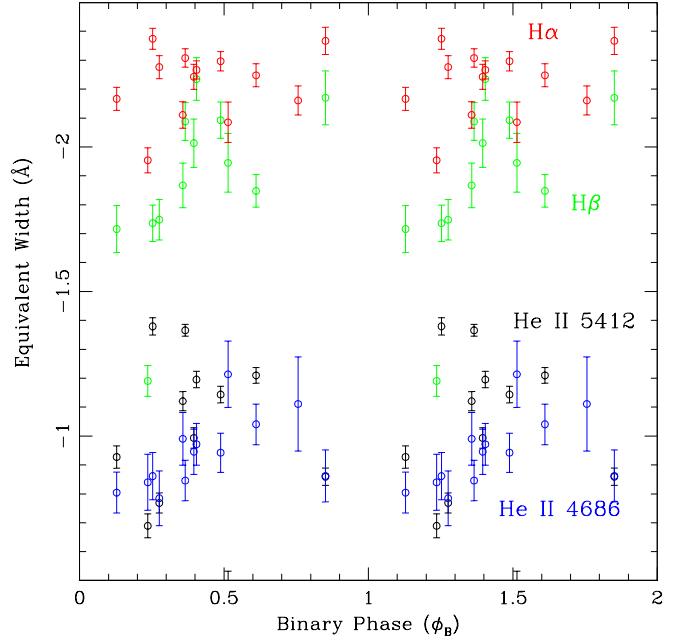| Species	λ_{rest} Å in air	Γ $\mathrm{km\,s^{-1}}$	χ^2/DoF	Log(Prob)
Hα	6562.808	43.0 ± 1.1	14.7	-3.9
Hβ	4861.34	22.4 ± 3.0	3.6	-1.2
Hγ	4340.48	25.5 ± 36.7	3.3	-1.2
He I	5875.65	72.9 ± 4.3	20.8	-5.3
He II	4685.682	44.1 ± 20.9	10.7	-3.0
He II	5411.52	63.3 ± 3.3	15.5	-4.1
He II	6527.099	125.8 ± 15.4	5.6	-1.7

FIG. 4.— Equivalent width and its variation for strong absorption lines. Hβ and He II 4686 absorption appears to weaken near phase $\phi_B = 0.2$.

is unclear how much of this variation is associated with the photosphere radial velocity. To illustrate, we average the radial velocity from the two strongest H I lines (Hα and Hβ) and two strongest He II lines ($\lambda4686$ and $\lambda5412$) and plot the values for the highest quality ($\mathrm{S/N}_{6000} > 20$) spectra (Figure 3). Even disregarding the mean radial velocity Γ offset between lines, we see that the fluctuations are several times the statistical error. Nevertheless, both sets of velocities show similar trends, with relatively low values in the range $\phi_B = 0.0 - 0.2$. Since $\phi_B = 0$ is the γ-/X-ray light curve maximum, it is tempting to identify this excursion with periastron and interpret the radial velocity measurements as showing significant eccentricity. The two species H I and He II show mean velocities $\Gamma_{\mathrm{H\,I}} = 31.9\,\mathrm{km\,s^{-1}}$ and $\Gamma_{\mathrm{He\,II}} = 46.2\,\mathrm{km\,s^{-1}}$ and RMS dispersions $\sigma_{\mathrm{H\,I}} = 11.1\,\mathrm{km\,s^{-1}}$ and $\sigma_{\mathrm{He\,II}} = 29.2\,\mathrm{km\,s^{-1}}$.

4.1. Equivalent Width Variations

Following Sarty et al. (2011), we checked the equivalent widths of our strongest absorption lines. Hα, the strongest atomic absorption has an average equivalent width of -2.2Å. Like these authors we also see evidence for equivalent width variation through the orbit, especially for Hβ and He II 4686 (Figure 4). However, in our case the minimum absorption strengths appear to lie at $\phi_B \approx 0.2$, close to compact object superior conjunction for the orbit suggested in figure 3 (i.e. when viewing the side of the companion away from the com-

pact object). This might indicate denser wind flow through the L3 point. Inspection of the strongest lines show variable wings, suggesting time or phase-dependent views of such outflow.

As for LS 5039, we find that our observed Hα equivalent width, -1.87 to -2.29Å, is smaller than the expected ≈ -3.27Å photospheric width for this spectral class (McSwain et al. 2004). Scaling from those authors' estimates (i.e. assuming similar companion mass and asymptotic wind velocity), we find that our lower observed residual absorption equivalent width implies a somewhat larger mass flux, namely $\dot{M} \approx 0.7 - 1.0 \times 10^{-7} M_\odot\,\mathrm{y}^{-1}$.

4.2. Radial Velocity Model and Implied Mass

Labeling the primary (compact object) 1 and the visible secondary 2, we have a single line spectroscopic binary, with radial velocity measurements constraining the mass function

$$f(M_1) = \frac{M_1^3}{(M_1 + M_2)^2}\sin^3 i = \frac{P}{2\pi G}K_2^3(1-e^2)^{\frac{3}{2}}$$

with $K_2 = \Delta v_2/2$ the radial velocity amplitude of the secondary and i the unknown system inclination. Since $\sin i < 1$ and $M_2 > 0$, $f(M_1)$ provides a lower bound to the mass of the primary. Casares et al. (2005) give the mass of an O6 V((f)) star as $20.0 - 26.4 M_\odot$.

In view of the large and poorly understood systematics, one should not directly fit our radial velocities. However, a basic model (figure 3) gives an idea of the allowed amplitude. Here a curve is plotted for $K = 40\mathrm{km\,s}^{-1}$, $\Gamma = 40\mathrm{km\,s}^{-1}$, $e = 0.2$, and longitude of ascending node $\omega = 0.6\pi$. This provides a reasonable match to the range of the He II line; the H I range is $K \approx 15\mathrm{km\,s}^{-1}$. Larger amplitudes or eccentricities provide a poor match to the data, so we take this as an upper limit on the allowed radial velocity amplitude. Sarty et al. (2011) adopt the He II radial velocity curve as minimizing wind contamination and best following the photospheric motion. Their curve for H I has a somewhat smaller amplitude than that for He II; for our data the range of H I velocities is $\sim 2.5\times$ smaller. Thus we follow Sarty et al. (2011) in adopting the He II velocities, but consider the possibility that these are systematics dominated and that the stronger H I lines reflect the true radial velocity amplitude.

Figure 5 shows the corresponding allowed regions in the mass-mass plane for circular orbits. For the allowed range of eccentricity M_1 will be up to 7% smaller. The solid lines show the $K = 40\mathrm{km\,s}^{-1}$ constraints suggested by He II, the dashed lines show the range from the Balmer lines.

5. DISCUSSION AND CONCLUSIONS

Our attempt to measure the radial velocity curve of 1FGL 1018.6−5856 has been frustrated by a large scatter, apparently due to systematic errors. In part these are certainly due to the imprecision of the continuum calibration in our echelle spectra. In part they are also likely due to variable absorption line components of a stellar wind unpredictably shifting the line centroids.

However, we do see that the maximum radial velocity amplitude allowed by our data is $\sim 40\mathrm{km\,s}^{-1}$. If this is the true radial velocity amplitude, then we would require a compact object mass $> 1.7 M_\odot$ and 50% of the allowed parameter space has $M_1 > 2.2 M_\odot$. Since the likely maximum neutron star mass is $\approx 2.5 M_\odot$, this would seem to suggest that the γ-ray source is a black hole. However, one should compare

with the masses of other stellar mass black holes. Farr et al. (2011) find that at 90% confidence the minimum M_{BH} in stellar mass binaries is $> 4.5 M_\odot$. Although they do not separately evaluate this for the high mass systems, like 1FGL 1018.6−5856, their figure 2 indicates most probable masses $10 - 20 M_\odot$ and 90% lower mass limits $> 10 M_\odot$. From figure 5 we see that we require $i < 30°$ for $M_1 > 4.5 M_\odot$ (a priori probability 13%), while for $M_1 > 10 M_\odot$ we require $i < 14°$ (probability 3%). Thus the likelihood of having a typical stellar black hole mass seems modest. When we consider that systematic errors may be contributing to the He II radial velocity width and that the H I radial velocity amplitude may be closer to the intrinsic amplitude, this only allows M_1 to exceed $4.5 M_\odot$ for $i < 11°$ (probability 2%). Thus we conclude that the modest radial velocity amplitude observed for 1FGL 1018.6−5856 prefers a neutron star. However, these statistical statements do not exclude either option and a clean measurement of the companion radial velocity would help the situation greatly.

The way forward on determining the mass of 1FGL J1018.6−5856 doubtless starts with improved spectroscopy. Our data show that the photospheric lines are quite broad, and likely variable. Accordingly a future campaign on small-medium class telescopes should obtain long-slit, moderate resolution ($R \sim 3000 - 6000$) spectra covering 4000-5500Å, with a collection of several template O6 V radial velocity comparisons. Queue/service observing is almost certainly required in view of the large P_b. Higher resolution echelle data from a large telescope can be of use, but will require higher S/N to allow deconvolution of the line shape and isolation of the systematic radial velocity. If the minimum mass exceeds $3 M_\odot$, we can be confident of a black hole primary. But in the more likely event that lower masses are allowed, the inclination becomes critical and one will require very high precision photometry to constrain the small ellipsoidal variations,
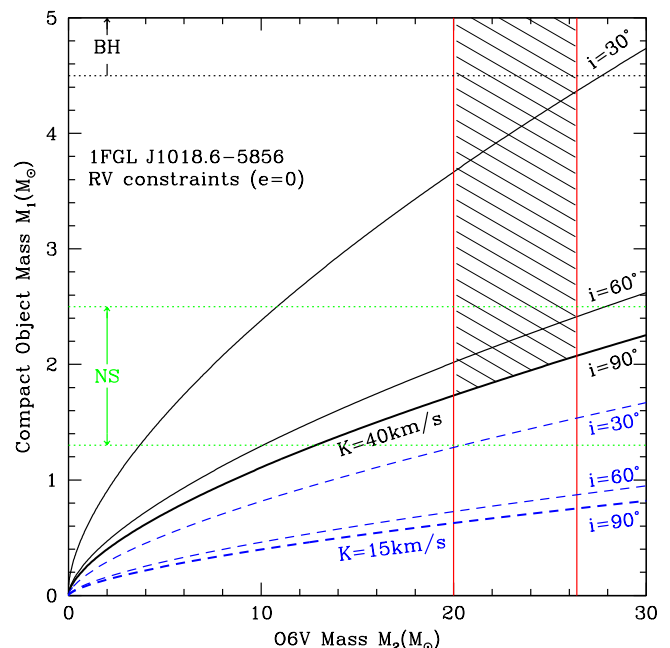

FIG. 5.— The binary mass-mass plane. For the He II-estimated radial velocity amplitude, we see that a neutron star (NS) solution requires small companion masses and/or large inclinations ($i > 50°$); roughly half of the allowed parameter space is consistent with a black hole (BH), although typical BH masses require very small inclinations. For the H I amplitude, a neutron star is highly preferred, requiring small inclinations to reach even $1.4 M_\odot$.

or constraints from light curve fitting at other wavebands.

REFERENCES

Ackermann, M. et al. 2012, Science, 335, 198
An, H.J., et al. 2013, ApJ, 775, 135
Casares, J., et al. 2005, MNRAS, 364, 899
Coley, J.B. et al. 2014, HEAD 1412210
Corbet, R. H. D. et al. 2011, ATEL #3221
Farr, W. M. et al. 2011, ApJ, 741, 103
Gray, R. O. 2009 "A Digital Spectral Classification Atlas v.1.07"
  (ned.ipac.caltech.edu/level5/Gray/Gray1.html)

Jascheck, P. & Jascheck, M. 1995, "The Behavior of Chemical Elements in
  Stars", (Cambridge University Press: Cambridge)
Jenniskens P. et al. 1996, AA, 313, 649
Kos, J. & Zwitter, T. 2013 ApJ 774 72
McSwain, M. V. et al. 2004, ApJ, 600, 927
Napoli, V.J. et al. 2011, PASP, 123, 1293
Parimucha, S. & Skoda, P. 2007, IAUS, 240, 486
Sarty, G.E. et al. 2011, MNRAS 411, 1293
Schwab, C. et al. 2010, SPIE conf. proc., 7735, 77354
Skoda, P. et al. 2008, SPIE conf. proc. 7014, 70145